Nano Research
2022, 15(6): 4873–4879

ISSN 1998-0124 CN 11-5974/O4
https://doi.org/10.1007/s12274-021-3805-1

Research Article

Magnetron co-sputtering synthesis and nanoindentation studies of nanocrystalline $(TiZrHf)_x(NbTa)_{1-x}$ high-entropy alloy thin films

Changjun Cheng[1], Xiaofu Zhang[2], Michel J. R. Haché[1], and Yu Zou[1] (✉)

[1] *Department of Materials Science and Engineering, University of Toronto, Toronto, Ontario M5S 3E4, Canada*
[2] *State Key Laboratory of Functional Materials for Informatics, Shanghai Institute of Microsystem and Information Technology and Center for Excellence in Superconducting Electronics, Chinese Academy of Sciences (CAS), Shanghai 200050, China*

Received: 27 June 2021 / **Revised:** 29 July 2021 / **Accepted:** 10 August 2021

ABSTRACT

Refractory high-entropy alloys (HEAs) possess many useful properties such as high strength and high-temperature stability. So far, most studies on refractory HEAs have been limited to a few well-known compositions and on their coarse-grain bulk forms. Here we fabricate nanocrystalline $(TiZrHf)_x(NbTa)_{1-x}$ HEA thin films with a large range of compositions (x = 0.07–0.90) by the direct current (DC) magnetron co-sputtering technique and measure their mechanical properties using the nanoindentation method. All the as-deposited HEA thin films show a solid-solution body-centered cubic (bcc) structure. As the compositional ratio (x) increases, the elastic modulus decreases from 153 to 123 GPa, following the trend of the rule of mixture. As x increases, the hardness first decreases from 6.5 GPa (x = 0.07) to the lowest value (4.6 GPa, x = 0.48) and then increases to the highest value (7.1 GPa, x = 0.90), showing a concave trend. The change in hardness might be attributed to the combinational influence caused by the atomic size and modulus effects, as well as the texture effect. The authors also propose a few open questions for future studies on this and related HEA systems.

KEYWORDS

high-entropy alloys, nanocrystalline alloys, refractory metals, thin films, magnetron co-sputtering, nanoindentation

1 Introduction

High-entropy alloys (HEAs) are an emerging class of metallic systems in which five or more principal elements form single or multiple solid-solution phases and show many useful properties [1–7]. Over the past two decades, researchers have made a significant advance in understanding face-centered cubic (fcc) HEAs [8], particularly Cantor alloys [2]. In the past decade, refractory HEAs (RHEAs)—a family of body-centered cubic (bcc) HEAs comprised of refractory elements from IVB (Ti, Zr, Hf), VB (V, Nb, Ta), VIB (Cr, Mo, W) groups—have attracted significant attention, due to their excellent mechanical properties and thermal stability [7, 9–15]. A large majority of RHEAs, such as NbMoTaW and NbMoTaWV [12], are rather brittle at room temperature, hindering their practical applications. As an exceptional example of RHEAs, TiZrHfNbTa systems exhibit superior ductility, even in their as-cast states [16–18]. In such a system, it is reported that adding the bcc NbTa binary alloy to the hexagonal close-packed (hcp) TiZrHf medium-entropy alloy (MEA) leads to a bcc phase [19, 20]. In addition, nanocrystalline $(TiZrHf)_x(NbTa)_{1-x}$ thin films (x: the compositional ratio) [20], prepared by the direct current (DC) magnetron co-sputtering technique, exhibit interesting electrical property transitions as x changes, including resistivity, superconducting transition temperature, and critical magnetic field, which have also been suggested in their bulk-state forms [21, 22]. The co-sputtering method can also be potentially used for fabricating HEA nanolattice structures for structural and functional applications [23, 24]. However, so far, the mechanical properties of the nanocrystalline $(TiZrHf)_x(NbTa)_{1-x}$ thin films have not been reported yet.

Furthermore, there have been few studies on the effect of a large range of compositional ratios (x) on the mechanical properties of the TiZrHfNbTa system. For bulk alloys composed of IVB- and VB-group elements, their yield strength and hardness do not always increase with increasing the configurational entropy (S_{mix}) [19, 25]: For example, TiHfNbTa (S_{mix} = 1.39R) exhibits lower yield strength and hardness than HfNbTa (S_{mix} = 1.10R). For a co-sputtered Ti-Zr-Nb system [26], the composition influences the morphology and texture of as-deposited thin films, but the correlation between its composition and mechanical properties is still not well understood. Moreover, due to the cocktail effect in HEAs [27], slight composition change may lead to a significant property variation. The equiatomic composition of the TiZrHfNbTa system may not exhibit the optimal combination of mechanical properties such as elastic modulus and hardness. Thus, two questions arise for the nanocrystalline $(TiZrHf)_x(NbTa)_{1-x}$ HEAs: (i) How does the compositional ratio influence their phase and microstructure? (ii) What are their mechanical properties over a large range of compositional ratios?

In this study, we fabricate nanocrystalline $(TiZrHf)_x(NbTa)_{1-x}$ HEA thin films within the composition series x = 0.07–0.90 and measure their elastic moduli (E) and hardness (H) using nanoindentation. Our results provide an improved understanding of phase stability, microstructure evolution, and mechanical properties of the nanocrystalline $(TiZrHf)_x(NbTa)_{1-x}$ RHEA system.

Address correspondence to mse.zou@utoronto.ca

2 Materials and experimental

To fabricate $(TiZrHf)_x(NbTa)_{1-x}$ thin films, we employed a DC magnetron co-sputtering system to co-deposit TiZrHf and TaNb (99.9%) on (100) oriented silicon wafers at room temperature. The compositional ratio was controlled by the power of each target; the substrate was rotated to ensure that the elements were homogeneously distributed. The detailed process was described in previous studies [15, 20]. Table S1 in the Electronic Supplementary Material (ESM) lists the corresponding fabrication parameters of the five samples with various compositional ratios. To make sure the compositional ratio (x) is uniform, the central regions of as-deposited films were selected and cut into ~ 5 mm × 5 mm samples for further characterization and nanomechanical testing.

The crystal structures and grain sizes of the as-deposited thin films were examined using the X-ray diffraction (XRD) method (D8 DISCOVER (Bruker) with Cu Kα1 wavelength). The surface morphology and element distribution of the films were characterized using a high-resolution scanning electron microscope (SEM, Hitachi SU5000) and its integrated energy dispersive X-ray spectroscopy (EDS, Bruker) at both 20 and 5 kV. We employed a nanoindenter (iMicro, KLA-Tencor) with a Berkovich tip to measure E and H using the continuous stiffness measurement (CSM) method in a displacement control mode. To reduce the effects from a blunt tip and substrates, we set the load maximum indentation depth as 200 nm, corresponding to a load of 11–16 mN. The measured E and H were calculated based on the Oliver-Pharr method [28, 29] and the Poisson's ratio of 0.402 [30]. The corrected E and H values that eliminate the substrate effect were calculated based on the modified King's model [31].

3 Results

Figure 1 shows the backscattered-electron (BSE) SEM images and EDS maps of the five samples and confirms that all the five elements (Ti, Zr, Hf, Nb, and Ta) are uniformly distributed. Table 1 lists the corresponding compositions for Samples #1–#5, with the x values of 0.07, 0.34, 0.48, 0.58, and 0.90, respectively. Figure 2 reveals the top surfaces and cross-sections of the five samples. The thickness of the as-deposited thin films is around 700 nm, except the sample #5 with a 1,094-nm thickness (Table 1). It is interesting to observe that the top surfaces of the thin films exhibit various visual features: For Samples #1 and #5, no obvious contrast is observed; for Sample #2, dendritic-like pattens are revealed; for Samples #3 and #4, dark dots in the size range of ~ 100 nm–1 μm are uniformly distributed. According to the SEM images of the film cross-sections, the roughness of the films also varies: (i) Sample #1 shows relatively high roughness; (ii) Sample #2 presents brick-like steps with the highest roughness among the samples; (iii) Samples #3 and #4 exhibit shallow sunken dimples

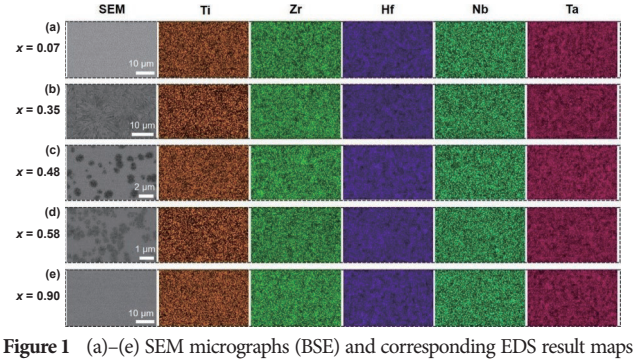

Figure 1 (a)–(e) SEM micrographs (BSE) and corresponding EDS result maps (20 kV) of the $(TiZrHf)_x(NbTa)_{1-x}$ HEA thin films, showing uniform elemental distributions.

Table 1 The compositions (at.%) and the corresponding x values of the $(TiZrHf)_x(NbTa)_{1-x}$ samples measured using the EDS (20 kV) as well as the thickness of the films measured in SEM images

No.	Ti (at.%)	Zr (at.%)	Hf (at.%)	Nb (at.%)	Ta (at.%)	x	Average thickness (nm)
1	2.6	1.9	2.8	44.4	48.3	0.07	756
2	12.1	9.7	12.0	34.3	31.8	0.34	688
3	19.7	12.6	15.3	26.6	25.8	0.48	659
4	20.3	21.9	16.3	19.0	22.5	0.58	771
5	36.7	25.2	28.4	5.2	4.5	0.90	1,094

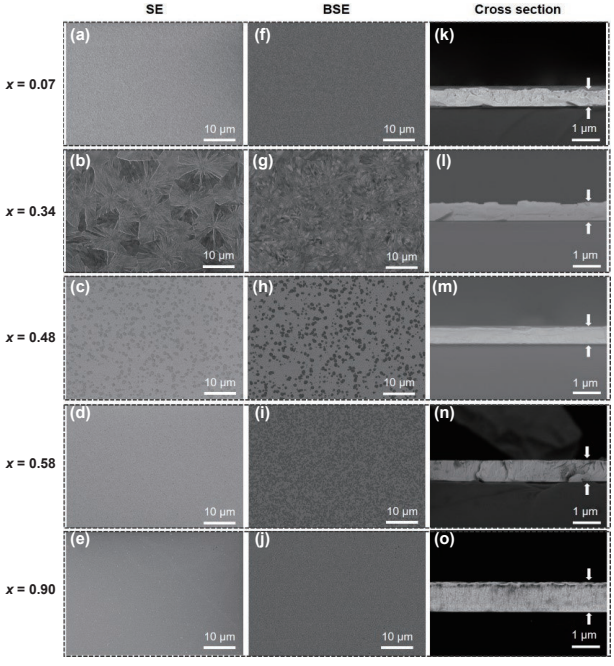

Figure 2 (a)–(e) Secondary electron (SE) and (f)–(o) BSE micrographs of the $(TiZrHf)_x(NbTa)_{1-x}$ HEA thin films: (a)–(j) top surfaces and (k)–(o) the cross-sections.

Table 2 The peak positions of (110) plane ($2\theta_{(100)}$), corresponding lattice constant, and calculated average grain size of the as-deposited $(TiZrHf)_x(NbTa)_{1-x}$ thin films according to the XRD results

No.	x	$2\theta_{(110)}$ (°)	Lattice constant (Å)	Grain size (nm)
1	0.07	38.2	3.329	21.1
2	0.34	38.02	3.344	33.0
3	0.48	37.46	3.393	22.0
4	0.58	37.2	3.415	29.2
5	0.9	36.02	3.523	21.1

(~ 100 nm depth), which may correspond to the dark dots observed on the top surface; (iv) Sample #5 shows a relatively flat surface. Despite various morphologies observed on these samples, we do not identify obvious element segregations in these films at both low (Figs. 1(a), 1(b), and 1(e)) and high (Figs. 1(c) and 1(d)) magnifications of the EDS maps.

The EDS point analysis at 5 kV on the dark dots of Samples #4 and #5 also confirms there is no obvious element segregation, including oxygen and carbon (Fig. S1 and Table S2 in the ESM). As shown in Fig. S1 in the ESM, some crack-like features are observed in Samples #3 and #4. The observed dark contrast features could be attributed to the surface roughness. In addition to the surface roughness effect, the formation of oxides on the thin films during or after the co-sputtering process may also result in distinct dark contrasts—a similar phenomenon has been reported

in Ref. [32]. Although there is no obvious oxygen and carbon accumulation observed in the EDS maps (Fig. S2 in the ESM), we are not able to eliminate the possibility of the formation of a very thin layer of oxides, because of the large interaction volume (~ 1 μm) of the characteristic X-rays.

Figure 3 shows the XRD patterns of as-prepared $(TiZrHf)_x(NbTa)_{1-x}$ HEA thin films: All the samples exhibit a bcc structure (Fig. 3(a)). As x increases, (110) peaks shift to a lower 2θ, indicating an increased lattice constant (Fig. 3(b)), which is in good agreement with Ref. [20]. Table 2 lists the corresponding (110) peak positions, lattice constants, and grain size for all five films. The measured lattice constant of Sample #4 (x = 0.58, 3.415 Å) is comparable to the reported values (3.404–3.414 Å [16, 33]). The grain size of the samples is around 20–30 nm. It is interesting to observe that Samples #1 and #5 exhibit a stronger (110) texture than the other samples.

Figure 4 shows the nanoindentation results for all the five samples. Figure 4(a) suggests the distinct E and H values among the samples. Figure 4(b) presents an obvious hardness drop and a curve serration at x = 0.48 and 0.58, respectively, which may result from the crack-like features in the dimples. Nevertheless, these features do not affect the mechanical properties in deeper regions, similar to the effect of roughness which is only valid at low depth during nanoindentation [34]. Figures 4(c) and 4(d) show the E and H values as a function of x. Based on the cross sections in Figs. 2(k)–2(o), the films with a relatively larger roughness (x = 0.07 and 0.34) present a higher level of scattering in E and H values than the other films. The shallow sunken dimples (x = 0.48 and 0.58) exhibit no obvious effect on data distribution. As shown in Fig. 4(c), the E values decrease as x increases, but the hardness shows a concave trend: The hardness shows relatively high "measured" values (~ 7.5–8.8 GPa) when x = 0.07 and 0.90, but it shows the lowest "measured" value (~ 6.3 GPa) when x = 0.48. The "corrected" values are obtained by eliminating the effect of the silicon substrate [31]; the "predicted" values are calculated according to the rule of mixtures. These are discussed in the following sections.

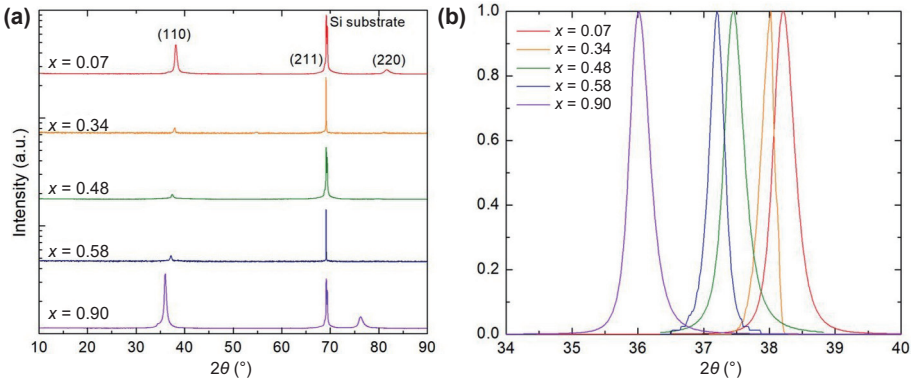

Figure 3 (a) XRD patterns of the as-deposited $(TiZrHf)_x(NbTa)_{1-x}$ thin films, indicating all the samples are single-phase bcc structured. Samples #1 and #5 show high intensities of (110), suggesting a strong (110) texture. (b) Normalized (110) peaks after deconvolution; the corresponding lattice constant and average grain size can be calculated accordingly. Note: in (a) it is difficult to identify the (211) peak of the samples due to the strong intensity from the silicon substrate.

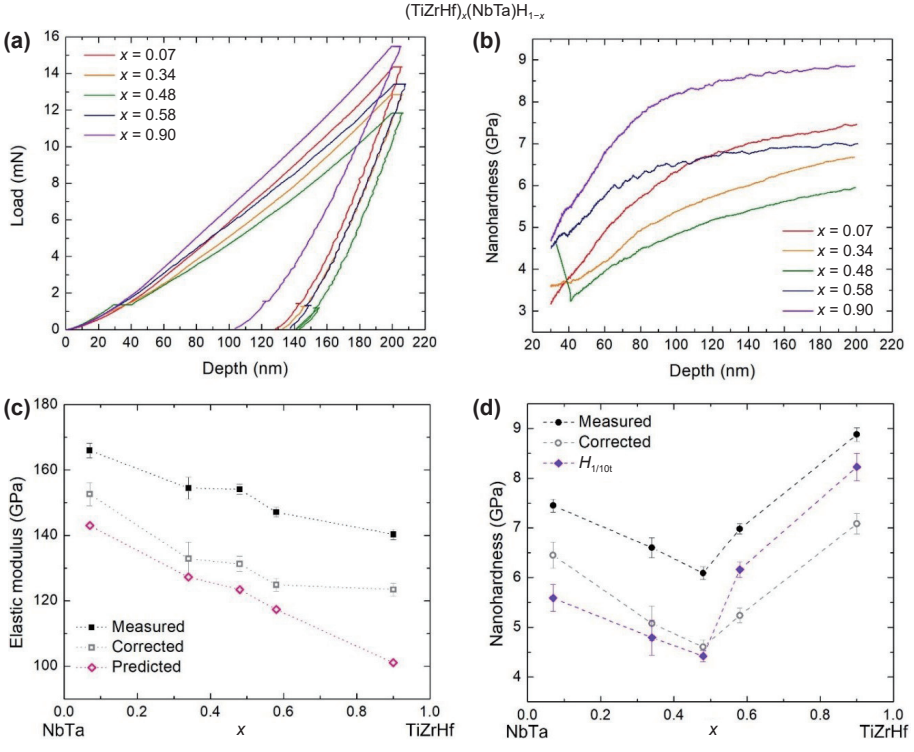

Figure 4 Nanoindentation testing of the HEA films: (a) representative load-displacement (depth) curves, (b) hardness-displacement curves, (c) elastic modulus (E) and (d) nanohardness (H) as a function of x. The measured values indicate the directly obtained results from the nanoindentation. The corrected values indicate the values that are eliminated from the substrate effect based on the modified King's model [31]. The predicted values indicate the calculated values according to the rule of mixture. The $H_{1/10t}$ values in (d) indicate the hardness obtained at the depth equal to 1/10 of the film thickness in the hardness-displacement curves.

4 Discussion

4.1 Formation of the single solid-solution bcc phase in $(TiZrHf)_x(NbTa)_{1-x}$ HEAs

As shown in Figs. 1–3, $(TiZrHf)_x(NbTa)_{1-x}$ HEAs present a single solid-solution bcc phase over a large composition range. Based on the modified Hume-Rothery rules, the thermodynamic parameters of configurational entropy ΔS_{mix}, mixing enthalpy ΔH_{mix}, and criterion Ω can be calculated as follows [35, 36]

$$\Delta S_{mix} = -R\sum c_i \ln(c_i) \quad (1)$$

$$\Delta H_{mix} = \sum 4\Delta H_{mix} c_i c_j \ (i \neq j) \quad (2)$$

$$\Omega = T_{mix}\Delta S_{mix}/\Delta H_{mix} \quad (3)$$

where R is the gas constant, c_i and c_j are the mole fraction of the element i and j, respectively, ΔH_{ij} is the enthalpy of mixing of binary liquid alloys [37], and T_{mix} is the melting point calculated based on the rule of mixture. The atomic-size difference δ, the electronegativity difference $\Delta\chi$, and the mixing valance electron concentration VEC_{mix} are determined as

$$\delta = [\sum c_i(1 - r_i/r_m)^2]^{0.5} \quad (4)$$

$$\Delta\chi = [\sum c_i(\chi_i - \chi_m)^2]^{0.5} \quad (5)$$

$$VEC_{mix} = \sum c_i VEC_i \quad (6)$$

where r_i, χ_i, and VEC_i are the atomic radius, the Pauling electronegativity, and the valence electron concentration of each element, respectively; r_m and χ_m are the average atomic radius and the average electronegativity, respectively, of component elements calculated by the rule of mixture.

Based on the properties of elements in Table 3 [17, 38–43], Table S3 in the ESM lists all the calculated results from Eqs. (1)–(6). To form single entropy-stabilized solid-solution phases, the criteria $\Omega > 1.1$, $\delta < 6.6\%$, and $\Delta\chi < 0.117$ are generally required for HEAs [36]. Meanwhile, the stable bcc phase exists in the range of $3 < VEC < 6.87$ [36]. Figure 5 shows the corresponding region of criteria δ, $\Delta\chi$, and VEC_{mix} as well as the data points of the samples in this study. Therefore, the fabricated HEA thin films present a single bcc phase based on the theoretical prediction, which is in good agreement with our experimental observations (Figs. 1–3).

4.2 The correction and relationship for E and H

In contrary to the literature [44–47], the measured E values in this study are significantly higher than that of the corresponding bulk HEAs [19, 25, 30, 33, 48]. This phenomenon could be due to the substrate effect during the nanoindentation of ~ 200 nm depth (h) on an approximate 700 nm-thick thin film [31, 49]. Generally, when the contact depth exceeds 10%–25% of the film thickness (t), the substrate effect should be considered [49], and there is an obvious transition for the slopes of hardness-displacement curves (Fig. 4(b)) at the depth of 65–110 nm, i.e., about 1/10 of the film thickness. Hence, we select the hardness data at the cutoff point $h/t = 10$, and the corresponding hardness ($H_{1/10t}$) shows a similar concave trend with lower values than the measured data (Fig. 4(d)).

Another way to eliminate the substrate effect is based on the modified King's model for Berkovich indenter [31]. The elastic modulus of the film (E_f) can be expressed as

$$1/E_r = (1-\nu_i^2)/E_i + (1-\nu_f^2)/E_f\left(1-e^{-\alpha(t-h)/a}\right) + (1-\nu_s^2)/E_s\left(e^{-\alpha(t-h)/a}\right) \quad (7)$$

where E_r is the reduced modulus, E_i and ν_i are the elastic modulus (1,140 GPa) and Poisson's ratio (0.07) of the diamond tip, E_s and ν_s are the elastic modulus (202 GPa) and Poisson's ratio (0.273) of the silicon substrate [50], a equals $24.56h^2$ for the Berkovich indenter, and α is a numerically determined scaling parameter (1.11–1.41 in our study and listed in Table S4 in the ESM [31]). The corresponding nanohardness can be calculated as

$$H = (4\beta/\pi)(P/S^2)E_r^2 \quad (8)$$

where P/S^2 is the load/stiffness^2 value measured during nanoindentation, β equals 1, and E_r is the calculated standard reduced modulus regardless of the substrate effect, i.e., $a/(t-h) \rightarrow 0$ [31].

Figures 4(c) and 4(d) and Table S4 in the ESM present all the data from the measurement, correction, and prediction. The corrected E values are about 10% higher than the values predicted by the rule of mixture and show the same trend as the prediction. The corrected H values (4.6–7.1 GPa) also correspond well to the reported H values at $x = 0.6$ (equiatomic, 4.97 GPa) [30] and $x = 1.0$ (6.02 GPa) [48]. The discrepancy between the corrected H and the $H_{1/10t}$ values may be attributed to the blunt Berkovich tip. The H values measured at the low depth will also be affected by the surface conditions (e.g., surface roughness) [34]. Therefore, the results are more reliable at a higher depth (> 100 nm), and the corrected H values could be more reliable than $H_{1/10t}$. The hardness of our nanocrystalline film samples is considerably higher than that tested in bulk-state TiZrHfNbTa HEAs (0.7–3 GPa) [19, 25, 33], which is due to the Hall-Petch effect (grain-boundary strengthening).

In addition, the parameter H/E can be used to classify different types of material [51–53]. As shown in Fig. 6, the H/E slopes vary for these materials: For pure metals (Ti, Zr, Hf, Nb, Ta) [33] and binary alloy (NbTa) [25], the slopes are relatively low ($H/E = 0.009$); for equiatomic TiZrHf MEAs [19, 48] and TiZrHfNbTa HEAs [19, 30, 33], the slope is much higher ($H/E = 0.0437$). Meanwhile, despite nano- and bulk-state HEAs being located at different H–E regions, they show comparable H/E

Table 3 Summary of the basic parameters of Ti, Zr, Hf, Nb, Ta: atomic size (r), melting point (T_m), Pauling electronegativity (χ), valence electron concentration (VEC), lattice constant (a), elastic modulus (E) and shear modulus (G)

Element	r (nm) [17]	T_m (K)	χ [38]	VEC	a (Å)bcc	E (GPa) [39]	G (GPa) [39]
Ti	0.142	1,933.15	1.54	4	3.282 [40]	120.2	45.6
Zr	0.157	2,125.15	1.33	4	3.5453[a]	98.0	35.0
Hf	0.155	2,423.15	1.30	4	3.543 [41]	141.0	56.0
Nb	0.143	2,741.15	1.60	5	3.3063 [42]	104.9	37.5
Ta	0.143	3,269.15	1.50	5	3.30276 [43]	185.7	69.2

[a]Data from PDF2-2004 (#34-0657).

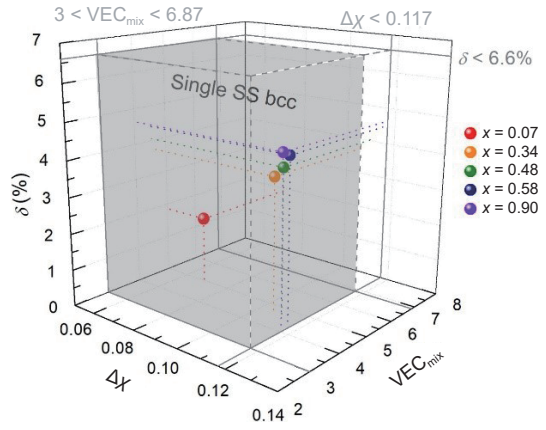

Figure 5 The criteria (grey box) of atomic size difference (δ), mixing valance electron concentration (VEC_{mix}), and electronegativity difference ($\Delta\chi$) to form a single solid-solution (SS) bcc phase. The colored data points represent the position of the HEA samples in this study.

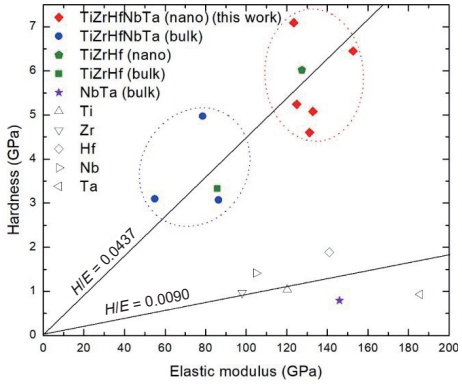

Figure 6 Relationship between elastic modulus and indentation hardness for pure elements (Ti, Zr, Hf, Nb, Ta) [33], binary alloy (NbTa) [25], MEA (TiZfHf) [19, 48], and HEAs (TiZrHfNbTa) [19, 30, 33] in both nanocrystalline and coarse-grain bulk forms. The blue and red dashed-line circles represent the data of coarse-grain and nanocrystalline HEAs, respectively.

slopes.

4.3 Mechanisms contributing to the hardness difference of the $(TiZrHf)_x(NbTa)_{1-x}$ HEAs

As the grain size of the samples is in a narrow range (20–30 nm), the Hall-Petch effect contributes little to the difference of hardness. Meanwhile, no secondary phase or intermetallic is observed in the samples. Here, we focus on solid-solution strengthening effects on the difference of hardness of the $(TiZrHf)_x(NbTa)_{1-x}$ HEAs. The corresponding solid-solution strengthening mechanism for HEAs was suggested by Senkov et al. [16] and modified by Yao et al. [54]. The increasing yield strength ($\Delta\sigma_i$) of element i can be estimated as

$$\Delta\sigma_i = G_{mix} A f_i^{4/3} c_i^{2/3} \quad (9)$$

where G_{mix} is the shear modulus of the alloy calculated by the rule of mixture [17], A is a material-dependent dimensionless parameter and equals 0.04 [16], and f_i is the interaction force parameter of element i and is related to shear modulus (G) and atomic size (r) [54]

$$f_i = [\delta_{G,i}^2 + (\beta\delta_{r,i})^2]^{0.5} \quad (10)$$

where β depends on the type of the mobile dislocation. In general, β ranges 2–4 for the screw dislocations and higher than 16 for edge dislocations [16]. Considering the random mixture of edge and screw dislocations in most alloys, the value of β equals 9 in this case [54].

For the single-phase bcc HEAs, each solute in the lattice has 8 nearest-neighbor atoms, forming a 9-atom cluster. Thus, the average differences of atomic modulus ($\delta_{G,i}$) and atomic size ($\delta_{r,i}$) with its neighbors can be determined as [16]

$$\delta_{G,i} = 9/8(\sum c_j \delta_{G,ij}) \quad (11)$$

$$\delta_{r,i} = 9/8(\sum c_j \delta_{r,ij}) \quad (12)$$

where $\delta_{G,ij} = 2(G_i - G_j)/(G_i + G_j)$ and $\delta_{r,ij} = 2(r_i - r_j)/(r_i + r_j)$. Hence, the solid-solution strengthening ($\Delta\sigma_{SS}$) can be obtained by the following equation [55]

$$\Delta\sigma_{SS} = (\sum \Delta\sigma_i^{1/q})^q \quad (13)$$

where q is the concentration exponent and equals 2/3 in Eq. (9) [54].

Generally, there is a nearly linear relationship between yield strength and hardness [56, 57], and here we assume that the values of $\Delta\sigma_{SS}$ and ΔH follow the same trend, i.e. $\Delta\sigma_{SS} \propto \Delta H$.

The local structural disorder and degree of lattice distortion can be estimated using the atomic displacement parameter (ADP), derived from the lattice parameter differences of the pure elements [14, 58]

$$ADP = \sum c_i (a_i - a_{al})^2 \quad (14)$$

where a_i is the lattice parameter of the pure elements and a_{al} is the lattice parameter of the alloy measured by the XRD (Table 2). Due to the pure bcc phase of the films, the bcc lattice constants of all elements are selected (Table 3). The corresponding ADP values increase as x increases (Table S5 in the ESM).

Based on Table 3, Eqs. (10) and (13), the solid-solution strengthening is contributed from the difference of shear modulus ($\Delta\sigma_{\delta G}$, modulus effect) and the lattice distortion ($\Delta\sigma_{\delta r}$, atomic size effect), which can be expressed as [54]

$$\Delta\sigma_{SS} = (\Delta\sigma_G^{3/2} + \Delta\sigma_r^{3/2})^{2/3} \quad (15)$$

The atomic size effect can be estimated by either $\Delta\sigma_{\delta r}$ or ADP. $\Delta\sigma_{\delta r}$ is calculated from theoretical radius values while ADP is based on both theoretical and measured lattice constants. ADP may reflect a more realistic trend of lattice distortion than the $\Delta\sigma_{\delta r}$, and the corresponding increment of strength ($\Delta\sigma_{ADP}$) can be estimated as

$$\Delta\sigma_{ADP} = G_{mix} A (\beta ADP^{0.5}/a_{al})^{4/3} \quad (16)$$

However, as the parameters A and β may not be suitable for Eq. (16), the contributions of $\Delta\sigma_{\delta G}$ and $\Delta\sigma_{ADP}$ cannot be directly summed to calculate $\Delta\sigma_{SS}$ by Eq. (13). As shown in Fig. 7, $\Delta\sigma_{\delta G}$ decreases as x increases, but both $\Delta\sigma_{\delta r}$ and $\Delta\sigma_{ADP}$ show a similar trend where the contribution of lattice distortion increases as x increases. The combination of these two effects may lead to the concave trend of hardness (Fig. 4). However, how these two effects in tandem influence the hardness is still required further investigation.

In addition, the preferred grain orientation (i.e., texture) may also affect the hardness. Based on the XRD results (Fig. 3), increasing the configurational entropy may result in a weak texture, which was also reported in Refs. [59, 60]. When the aggregation of the oriented grain becomes stronger, the strength and hardness may increase [61–63]. Nevertheless, for a bcc system with low anisotropy, the grain-orientation effect on the modulus and hardness might be minor.

5 Conclusions

In this study, we have fabricated nanocrystalline (20–30 nm)

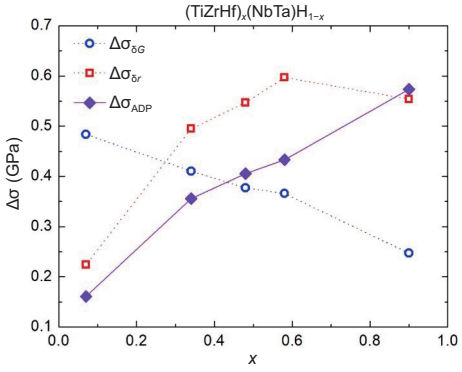

Figure 7 The increment of the strength ($\Delta\sigma$) that is attributed to the shear modulus difference ($\Delta\sigma_{\delta G}$), atomic radius difference ($\Delta\sigma_{\delta r}$), and lattice distortion ($\Delta\sigma_{ADP}$) as a function of the compositional ratio (x).

$(TiZrHf)_x(NbTa)_{1-x}$ HEA thin films within a large composition range (x = 0.07–0.90). All the samples show a single solid-solution bcc phase with a homogeneous element distribution. The samples with x = 0.07 and 0.90 show stronger (110) texture than the samples with x = 0.34, 0.48, and 0.58, while the latter ones reveal higher surface contrasts than the former ones. As x increases, the elastic moduli of the films decrease from 153 to 123 GPa, following the trend of the rule of mixture. For the hardness, as x increases, the hardness first decreases from 6.5 GPa (x = 0.07) to 4.6 GPa (x = 0.48, the lowest value), and then the hardness increases to 7.1 GPa (the highest value). Such concave trend of hardness is mainly attributed to both atomic size and modulus effects on solid-solution strengthening. The texture and surface morphologies may also play minor roles.

A few open questions are interesting for future investigation: (i) the effect of compositions and S_{mix} on the texture and surface morphology of as-deposited $(TiZrHf)_x(NbTa)_{1-x}$ thin films; (ii) the fundamental understanding and calculation of atomic size and modulus effects (and probably long- or short-range ordering effects) on the strengthening of the $(TiZrHf)_x(NbTa)_{1-x}$ system.

Acknowledgements

The authors thank Dr. Yanan Liu (Department of Earth Sciences, University of Toronto) and Mr. Zhiying Liu (Department of Materials Science and Engineering, University of Toronto) for their experimental support and helpful discussion; J. Wei for his assistance with the preparation of the graphic abstract; Minh-Tam Nguyen for proofreading the manuscript. Y. Z. acknowledges the financial support from the Discovery Grants Program (No. RGPIN-2018-05731) of the Natural Sciences and Engineering Research Council of Canada (NSERC), New Frontiers in Research Fund - Exploration (No. NFRFE-2019-00603), and Dean's Spark Assistant Professorship in the Faculty of Applied Science & Engineering at the University of Toronto. M. J. R. H. acknowledges the financial support from Vanier Canada Graduate Scholarship (NSERC), Ontario Graduate Scholarship, and Queen Elizabeth II/Eleanor and Burnett Thall Graduate Scholarship, and Canada Foundation for Innovation (CFI)-John R. Evans Leaders Fund (JELF) Project# 38044.

Electronic Supplementary Material: Supplementary materials (SEM images with corresponding carbon and oxygen distribution, fabrication parameters, EDS results at low voltage, calculated thermodynamics and structure criteria, measured, corrected, and predicted nanoindentation results, and calculated solid solution strengthening effects) is available in the online version of this article at https://doi.org/10.1007/s12274-021-3805-1.

References

[1] Yeh, J. W.; Chen, S. K.; Lin, S. J.; Gan, J. Y.; Chin, T. S.; Shun, T. T.; Tsau, C. H.; Chang, S. Y. Nanostructured high-entropy alloys with multiple principal elements: Novel alloy design concepts and outcomes. *Adv. Eng. Mater.* **2004**, *6*, 299–303.

[2] Cantor, B.; Chang, I. T. H.; Knight, P.; Vincent, A. J. B. Microstructural development in equiatomic multicomponent alloys. *Mater. Sci. Eng.: A* **2004**, *375-377*, 213–218.

[3] Zhang, Y.; Zuo, T. T.; Tang, Z.; Gao, M. C.; Dahmen, K. A.; Liaw, P. K.; Lu, Z. P. Microstructures and properties of high-entropy alloys. *Prog. Mater. Sci.* **2014**, *61*, 1–93.

[4] Ye, Y. F.; Wang, Q.; Lu, J.; Liu, C. T.; Yang, Y. High-entropy alloy: Challenges and prospects. *Mater. Today* **2016**, *19*, 349–362.

[5] Miracle, D. B.; Senkov, O. N. A critical review of high entropy alloys and related concepts. *Acta Mater.* **2017**, *122*, 448–511.

[6] Gao, M. C.; Miracle, D. B.; Maurice, D.; Yan, X. H.; Zhang, Y.; Hawk, J. A. High-entropy functional materials. *J. Mater. Res.* **2018**, *33*, 3138–3155.

[7] Haché, M. J. R.; Cheng, C. J.; Zou, Y. Nanostructured high-entropy materials. *J. Mater. Res.* **2020**, *35*, 1051–1075.

[8] Wu, Z.; Bei, H.; Pharr, G. M.; George, E. P. Temperature dependence of the mechanical properties of equiatomic solid solution alloys with face-centered cubic crystal structures. *Acta Mater.* **2014**, *81*, 428–441.

[9] Senkov, O. N.; Wilks, G. B.; Miracle, D. B.; Chuang, C. P.; Liaw, P. K. Refractory high-entropy alloys. *Intermetallics* **2010**, *18*, 1758–1765.

[10] Sheikh, S.; Shafeie, S.; Hu, Q.; Ahlström, J.; Persson, C.; Veselý, J.; Zýka, J.; Klement, U.; Guo, S. Alloy design for intrinsically ductile refractory high-entropy alloys. *J. Appl. Phys.* **2016**, *120*, 164902.

[11] Feng, X. B.; Zhang, J. Y.; Xia, Z. R.; Fu, W.; Wu, K.; Liu, G.; Sun, J. Stable nanocrystalline NbMoTaW high entropy alloy thin films with excellent mechanical and electrical properties. *Mater. Lett.* **2018**, *210*, 84–87.

[12] Senkov, O. N.; Wilks, G. B.; Scott, J. M.; Miracle, D. B. Mechanical properties of $Nb_{25}Mo_{25}Ta_{25}W_{25}$ and $V_{20}Nb_{20}Mo_{20}Ta_{20}W_{20}$ refractory high entropy alloys. *Intermetallics* **2011**, *19*, 698–706.

[13] Zou, Y.; Wheeler, J. M.; Ma, H.; Okle, P.; Spolenak, R. Nanocrystalline high-entropy alloys: A new paradigm in high-temperature strength and stability. *Nano Lett.* **2017**, *17*, 1569–1574.

[14] Zou, Y.; Maiti, S.; Steurer, W.; Spolenak, R. Size-dependent plasticity in an $Nb_{25}Mo_{25}Ta_{25}W_{25}$ refractory high-entropy alloy. *Acta Mater.* **2014**, *65*, 85–97.

[15] Zou, Y.; Ma, H.; Spolenak, R. Ultrastrong ductile and stable high-entropy alloys at small scales. *Nat. Commun.* **2015**, *6*, 7748.

[16] Senkov, O. N.; Scott, J. M.; Senkova, S. V.; Miracle, D. B.; Woodward, C. F. Microstructure and room temperature properties of a high-entropy TaNbHfZrTi alloy. *J. Alloys Compd.* **2011**, *509*, 6043–6048.

[17] Tseng, K. K.; Juan, C. C.; Tso, S.; Chen, H. C.; Tsai, C. W.; Yeh, J. W. Effects of Mo, Nb, Ta, Ti, and Zr on mechanical properties of equiatomic Hf-Mo-Nb-Ta-Ti-Zr alloys. *Entropy* **2019**, *21*, 15.

[18] Hu, M. L.; Song, W. D.; Duan, D. B.; Wu, Y. Dynamic behavior and microstructure characterization of TaNbHfZrTi high-entropy alloy at a wide range of strain rates and temperatures. *Int. J. Mech. Sci.* **2020**, *182*, 105738.

[19] Wang, S. B.; Wu, D. L.; She, H.; Wu, M. X.; Shu, D.; Dong, A. P.; Lai, H. C.; Sun, B. D. Design of high-ductile medium entropy alloys for dental implants. *Mater. Sci. Eng.: C* **2020**, *113*, 110959.

[20] Zhang, X. F.; Winter, N.; Witteveen, C.; Moehl, T.; Xiao, Y.; Krogh, F.; Schilling, A.; Von Rohr, F. O. Preparation and characterization of high-entropy alloy $(TaNb)_{1-x}(ZrHfTi)_x$ superconducting films. *Phys. Rev. Res.* **2020**, *2*, 013375.

[21] Von Rohr, F.; Winiarski, M. J.; Tao, J.; Klimczuk, T.; Cava, R. J. Effect of electron count and chemical complexity in the Ta-Nb-Hf-Zr-Ti high-entropy alloy superconductor. *Proc. Natl. Acad. Sci. USA* **2016**, *113*, E7144–E7150.

[22] Guo, J.; Wang, H. H.; Von Rohr, F.; Wang, Z.; Cai, S.; Zhou, Y. Z.; Yang, K.; Li, A. G.; Jiang, S.; Wu, Q. et al. Robust zero resistance in a superconducting high-entropy alloy at pressures up to 190 GPa.

Proc. Natl. Acad. Sci. USA **2017**, *114*, 13144–13147.
[23] Feng, X. B.; Surjadi, J. U.; Fan, R.; Li, X. C.; Zhou, W. Z.; Zhao, S. J.; Lu, Y. Microalloyed medium-entropy alloy (MEA) composite nanolattices with ultrahigh toughness and cyclability. *Mater. Today* **2021**, *42*, 10–16.
[24] Surjadi, J. U.; Feng, X. B.; Fan, R.; Lin, W. T.; Li, X. C.; Lu, Y. Hollow medium-entropy alloy nanolattices with ultrahigh energy absorption and resilience. *NPG Asia Mater.* **2021**, *13*, 36.
[25] Wang, S. P.; Ma, E.; Xu, J. New ternary equi-atomic refractory medium-entropy alloys with tensile ductility: Hafnium versus titanium into NbTa-based solution. *Intermetallics* **2019**, *107*, 15–23.
[26] Yan, X. H.; Ma, J.; Zhang, Y. High-throughput screening for biomedical applications in a Ti-Zr-Nb alloy system through masking co-sputtering. *Sci. China Phys. Mech. Astron.* **2019**, *62*, 996111.
[27] Yeh, J. W. Recent progress in high-entropy alloys. *Ann. Chim. Sci. Mat.* **2006**, *31*, 633–648.
[28] Oliver, W. C.; Pharr, G. M. Measurement of hardness and elastic modulus by instrumented indentation: Advances in understanding and refinements to methodology. *J. Mater. Res.* **2004**, *19*, 3.
[29] Oliver, W. C.; Pharr, G. M. An improved technique for determining hardness and elastic modulus using load and displacement sensing indentation experiments. *J. Mater. Res.* **1992**, *7*, 1564–1583.
[30] Dirras, G.; Lilensten, L.; Djemia, P.; Laurent-Brocq, M.; Tingaud, D.; Couzinié, J. P.; Perrière, L.; Chauveau, T.; Guillot, I. Elastic and plastic properties of as-cast equimolar TiHfZrTaNb high-entropy alloy. *Mater. Sci. Eng.: A* **2016**, *654*, 30–38.
[31] Saha, R.; Nix, W. D. Effects of the substrate on the determination of thin film mechanical properties by nanoindentation. *Acta Mater.* **2002**, *50*, 23–38.
[32] Ma, H. Microstructure engineering via ion-irradiation in metallic thin films. Ph.D. Dissertation, ETH Zurich, 2017.
[33] Lin, C. M.; Juan, C. C.; Chang, C. H.; Tsai, C. W.; Yeh, J. W. Effect of Al addition on mechanical properties and microstructure of refractory $Al_xHfNbTaTiZr$ alloys. *J. Alloys Compd.* **2015**, *624*, 100–107.
[34] Jia, Y. F.; Cui, Y. Y.; Xuan, F. Z.; Yang, F. Q. Comparison between single loading-unloading indentation and continuous stiffness indentation. *RSC Adv.* **2017**, *7*, 35655–35665.
[35] Takeuchi, A.; Inoue, A. Quantitative evaluation of critical cooling rate for metallic glasses. *Mater. Sci. Eng.: A* **2001**, *304-306*, 446–451.
[36] Nutor, R. K.; Cao, Q. P.; Wang, X. D.; Zhang, D. X.; Fang, Y. Z.; Zhang, Y.; Jiang, J. Z. Phase selection, lattice distortions, and mechanical properties in high-entropy alloys. *Adv. Eng. Mater.* **2020**, *22*, 2000466.
[37] Takeuchi, A.; Inoue, A. Classification of bulk metallic glasses by atomic size difference, heat of mixing and period of constituent elements and its application to characterization of the main alloying element. *Mater. Trans.* **2005**, *46*, 2817–2829.
[38] Emsley, J. *The Elements*, 3rd ed.; Clarendon Press: Oxford, 1998.
[39] Gale, W. F.; Totemeier, T. C. *Smithells Metals Reference Book*, 8th ed.; Elsevier Science: Amsterdam, 2003.
[40] Levinger, B. W. Lattice parameter of beta Titanium at room temperature. *JOM* **1953**, *5*, 195.
[41] Hao, Y. J.; Zhu, J.; Zhang, L.; Ren, H. S.; Qu, J. Y. Structure phase transition and elastic properties of hafnium: First-principles study. *Philos. Mag. Lett.* **2011**, *91*, 61–69.
[42] Roberge, R. Lattice parameter of niobium between 4.2 and 300 K. *J. Less Common Met.* **1975**, *40*, 161–164.
[43] Mueller, M. H. The lattice parameter of tantalum. *Scr. Mater.* **1977**, *11*, 693.
[44] Goyal, M.; Gupta, B. R. K. Study of shape, size and temperature-dependent elastic properties of nanomaterials. *Mod. Phys. Lett. B* **2019**, *33*, 1950310.
[45] Kumar, R.; Kumar, M. Size dependence of thermoelastic properties of nanomaterials. *Int. J. Nanosci.* **2010**, *9*, 537–542.
[46] Sun, C. T.; Zhang, H. T. Size-dependent elastic moduli of platelike nanomaterials. *J. Appl. Phys.* **2003**, *93*, 1212–1218.
[47] Wang, J.; Huang, Q. A.; Yu, H. Size and temperature dependence of Young's modulus of a silicon nano-plate. *J. Phys. D: Appl. Phys.* **2008**, *41*, 165406.
[48] Meng, H.; Duan, J. M.; Chen, X. T.; Jiang, S.; Shao, L.; Tang, B. Y. Influence of local lattice distortion on elastic properties of hexagonal close-packed TiZrHf and TiZrHfSc refractory alloys. *Phys. Status Solidi B* **2021**, *258*, 2100025.
[49] Pharr, G. M.; Oliver, W. C. Measurement of thin film mechanical properties using nanoindentation. *MRS Bull.* **1992**, *17*, 28–33.
[50] Bhushan, B.; Li, X. D. Micromechanical and tribological characterization of doped single-crystal silicon and polysilicon films for microelectromechanical systems devices. *J. Mater. Res.* **1997**, *12*, 54–63.
[51] Bolshakov, A.; Pharr, G. M. Influences of pileup on the measurement of mechanical properties by load and depth sensing indentation techniques. *J. Mater. Res.* **1998**, *13*, 1049–1058.
[52] Sun, W. J.; Kothari, S.; Sun, C. C. The relationship among tensile strength, Young's modulus, and indentation hardness of pharmaceutical compacts. *Powder Technol.* **2018**, *331*, 1–6.
[53] Wheeler, J. M. Mechanical phase mapping of the Taza meteorite using correlated high-speed nanoindentation and EDX. *J. Mater. Res.* **2021**, *36*, 94–104.
[54] Yao, H. W.; Qiao, J. W.; Hawk, J. A.; Zhou, H. F.; Chen, M. W.; Gao, M. C. Mechanical properties of refractory high-entropy alloys: Experiments and modeling. *J. Alloys Compd.* **2017**, *696*, 1139–1150.
[55] Gypen, L. A.; Deruyttere, A. Multi-component solid solution hardening. *J. Mater. Sci.* **1977**, *12*, 1028–1033.
[56] Toda-Caraballo, I.; Rivera-Díaz-del-Castillo, P. E. J. Modelling solid solution hardening in high entropy alloys. *Acta Mater.* **2015**, *85*, 14–23.
[57] Rice, P. M.; Stoller, R. E. Correlation of nanoindentation and conventional mechanical property measurements. *MRS Online Proc. Libr.* **2000**, *649*, 711.
[58] Maiti, S.; Steurer, W. Structural-disorder and its effect on mechanical properties in single-phase TaNbHfZr high-entropy alloy. *Acta Mater.* **2016**, *106*, 87–97.
[59] Vüllers, F. T. N.; Spolenak, R. From solid solutions to fully phase separated interpenetrating networks in sputter deposited "immiscible" W-Cu thin films. *Acta Mater.* **2015**, *99*, 213–227.
[60] Müller, C. M.; Parviainen, S.; Djurabekova, F.; Nordlund, K.; Spolenak, R. The as-deposited structure of co-sputtered Cu-Ta alloys, studied by X-ray diffraction and molecular dynamics simulations. *Acta Mater.* **2015**, *82*, 51–63.
[61] Lin, N.; Liu, S. F.; Liu, Y. H.; Fan, H. Y.; Zhu, J. L.; Deng, C.; Liu, Q. Effects of asymmetrical rolling on through-thickness microstructure and texture of body-centered cubic (BCC) tantalum. *Int. J. Refract. Met. Hard Mater.* **2019**, *78*, 51–60.
[62] Chou, W. J.; Yu, G. P.; Huang, J. H. Mechanical properties of TiN thin film coatings on 304 stainless steel substrates. *Surf. Coat. Technol.* **2002**, *149*, 7–13.
[63] Meng, Q. N.; Wen, M.; Qu, C. Q.; Hu, C. Q.; Zheng, W. T. Preferred orientation, phase transition and hardness for sputtered zirconium nitride films grown at different substrate biases. *Surf. Coat. Technol.* **2011**, *205*, 2865–2870.